ADVANCED MATERIALS TECHNOLOGIES

www.advmattechnol.de

3D Printing of Amylopectin-Based Natural Fiber Composites

*Yijie Jiang and Jordan R. Raney**

Many ancient Chinese structures, such as portions of the Great Wall, use a unique mortar that derives from glutinous rice (commonly called "sticky rice"). Unlike other types of rice, sticky rice is rich in amylopectin with negligible amylose. Inspired by the long-term stability of the amylopectin-based mortars in ancient structures, sticky rice (SR)-based materials for 3D printing are developed. Heat causes amylopectin gelatinization, during which molecular branches open to form a large network of gel balls. This causes a merger of the granules and improved interaction between the matrix and fillers. To enhance the mechanical properties, cotton fibers are included, ≈11 μm in diameter. During amylopectin gelatinization, secondary fibers emerge from the primary fibers, creating a complex two-level fiber network. Both the fibers and matrix constitute a 3D printable fiber composite consisting entirely of natural, inexpensive, and scalable components. The processing steps make no use of any non-natural materials or hazardous chemicals. A systematic design of experiments is conducted to understand the effect of processing parameters on the mechanical properties. Scalability by printing low-density cellular materials is demonstrated. Finally, it is shown that SR composites are more resilient than common thermoplastic composites when subjected to flame, heat, or ultraviolet light.

1. Introduction

Many ancient structures in China (since 386–589 AD), including the Great Wall, have been found to contain a unique mortar that was derived from sticky rice.[1,2] Unlike many kinds of rice that are a mix of amylose and amylopectin, sticky rice consists of pure amylopectin, a highly branched polymer with double helical, crystalline structures formed in short branched chains[3] (**Figure 1**a). With proper water content and thermal processing, sticky rice undergoes gelatinization,[3,4] during which branches open to form a large network of gel balls.[5] Subsequent retrogradation, i.e., the recrystallization of the amylopectin branches back to dual helical crystals, provides resistance to both enzymatic and acid hydrolysis[3,4] of sticky rice-based materials. Mortar based on sticky rice shows increased stiffness and strength and reduced density and shrinkage[1,6] relative to pure lime mortar.

There is growing interest in developing natural materials for additive manufacturing as renewable, recyclable, and environmentally safe alternatives to the materials currently in use.[7–14] Natural materials, such as starch,[7–9] have been used in 3D printing. However, these are typically not designed for load-bearing use. For example, 3D printed corn starch has low stiffness (34 MPa)[8] and is used as a temporary sacrificial material.[7]

Here, inspired by the long-term stability of sticky rice-based mortar in ancient Chinese structures, we design 3D-printable, all-natural composites based on sticky rice (SR) and cotton linter fibers (CL). Natural fibers obtained from plants (e.g., bamboo, flax, etc.) are a renewable and sustainable resource. The major components of natural fibers are cellulose, hemicellulose, and lignin.[15,16] Each type of natural fiber has different ratios of these components, and thus different properties, such as mechanical strength, density, moisture absorption, and degradation under exposure to heat or ultraviolet light.[15,17–22] Natural fibers such as cellulose have been previously used in thermoplastic or thermoset matrices.[15,22–24] These composites have been processed both using traditional manufacturing methods (including compression molding,[24] extrusion,[25,26] injection molding,[26,27] and resin transfer molding[28]) and 3D printing (e.g., wood fibers in thermoplastic matrices[13,29]). However, combining the natural fibers with highly processed synthetic polymers often requires chemical treatment of the fiber surfaces[30] to improve fiber–matrix interaction. In contrast, natural matrix materials are already compatible with natural fibers. In this work, we use short cotton fibers to improve the mechanical properties of the amylopectin matrix. These natural fibers have a high strain of failure and have a strength similar to other natural fibers.[30] The cotton forms a network of primary fibers (with diameters of ≈11 μm), which are nominally aligned along the print path due to shearing of the material during extrusion,[10,31,32] and secondary (submicron) fibers that emerge from the surfaces of the primary fibers. We investigate the effect of processing parameters on the microstructure and the mechanical properties using formal design of experiments (DOE). We compare the properties of the SR-based composites to those of commercial thermoplastic-based fiber composites (PLA-wood fibers). We find that the SR-based composites

Dr. Y. Jiang, Prof. J. R. Raney
Department of Mechanical Engineering and Applied Mechanics
University of Pennsylvania
Philadelphia, PA 19104, USA
E-mail: raney@seas.upenn.edu

The ORCID identification number(s) for the author(s) of this article can be found under https://doi.org/10.1002/admt.201900521.

DOI: 10.1002/admt.201900521

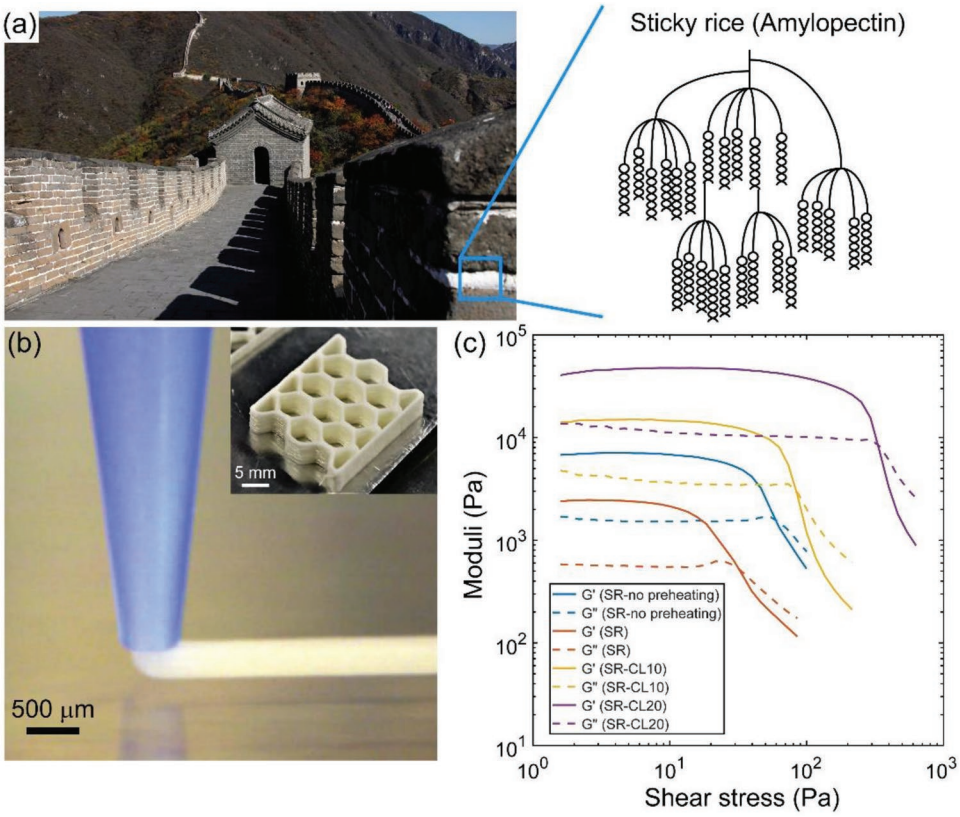

Figure 1. a) A schematic of highly branched structures of amylopectin, the primary component in sticky rice, and its application as a mortar in building the ancient Great Wall (photo Reuters Pictures; used with permission). b) Extrusion of SR-CL10 ink during DIW and a printed cellular sample in inset. c) Rheology measurements of pure SR (with and without preheating), SR-CL10 and SR-CL20 inks show yielding behavior, which is desirable for printability.

show comparable stiffness (≈2 GPa) but are more fire retardant, and more resistant to degradation during exposure to UV or high temperatures. Additionally, these sustainable composites, which are entirely made from renewable and natural materials, are inexpensive, scalable, and biodegradable without any hazardous components. This opens up broader possible applications in food and medicine.

2. Results and Discussions

To 3D print the natural composites in this study we use direct ink writing (DIW), a printing method in which non-Newtonian inks are extruded from a translating nozzle at ambient conditions.[33,34] This approach offers an unprecedented palette of compatible materials.[34,35] To produce the composite inks, we use only SR (powder), water, and cotton fibers, without any other chemical or binders. The components are first added in the ratios shown in **Table 1**, then mixed and subjected to a thermal treatment (at temperature T_{Pre} discussed below), causing gelatinization of amylopectin (details in the Experimental Section).[4] During gelatinization, helical branch chains expand as gel balls and interact with fillers via hydrogen bonding. Figure 1b shows printing of the SR composite with 10 wt% cotton fibers (SR-CL10) from a 400 μm nozzle and (inset) a cellular structure printed via this process. The composite inks are shear-thinning (Figure S1, Supporting Information) and possesses a viscoelastic yield stress (Figure 1c), as desired for direct write processes.[31,36] Whether the material can be easily extruded and subsequently maintain its shape after extrusion depends most strongly on the quantity of water (Figure S2, Supporting Information). The ideal water content ranges between C_{Water} = 50 and 56 wt%. Above this, the inks spread after extrusion, not stacking or maintaining shape; below this, the inks can become clogged during extrusion. The preheating temperature T_{Pre} shows a less significant effect on printability over the range of 60 to 140 °C (Figure S2, Supporting Information). After printing the samples, a freeze-drying process and post-printing thermal treatment (at temperature T_{Post}, see details in the

Table 1. Ratio of components by weight for ink preparation.

Inks	SR	CL	Water
SR (without preheating)	1	0	0.93
SR	1	0	0.98
SR-CL10	1	0.11	1.25
SR-CL12	1	0.14	1.35
SR-CL15	1	0.18	1.45
SR-CL18	1	0.22	1.55
SR-CL20	1	0.25	1.63

Table 2. Parameter levels in Taguchi DOE. The processing parameters at three different levels are investigated.

Parameter	Level 1	Level 2	Level 3
T_{Pre} [°C]	80	100	120
C_{Water} [wt%]	50	53	56
T_{Post} [°C]	90	120	150

Experimental Section) are performed to remove water, solidifying the material.

To characterize the mechanical properties of the materials, we first 3D printed tensile specimens using a print path parallel with the subsequent direction of applied load, to orient the fiber bundles predominantly along the direction of loading ("longitudinal"). Using a commercial quasistatic test system, tensile tests were performed to measure the stiffness and strength of the samples. To determine the effect of processing parameters on the mechanical properties of the final, post-processed material, we performed a Taguchi design of experiments[37] with three parameters: preheating temperature (T_{Pre}), initial water content (C_{Water}), and post-printing temperature (T_{Post}). For each parameter three different values were selected (**Table 2**). In Taguchi DOE, an array of experiments comprising orthogonal combinations of the different levels of parameters is generated to correlate the effects of the chosen parameters with the final properties, while minimizing the number of experiments. This array is called an L9 orthogonal table, as listed in Table S1 (Supporting Information). As shown in **Figure 2**a,b, stiffness and strength increase significantly with increasing levels of T_{Pre} but vary only slightly with the other two parameters. The contribution of T_{Pre} accounts for 95% and 89% of the variation of stiffness and strength, respectively. The stiffness ranges from 688 MPa to 1.88 GPa and the strength ranges from 10.5 MPa to 19.9 MPa as a function of T_{Pre}. The large dependence of the mechanical properties on T_{Pre} appears to result from the strong effect of T_{Pre} on the microstructure of the printed materials. Figure 2c–h shows scanning electron microscope (SEM) images of the surface of our manufactured SR-based materials, revealing granular-like surface features. The granules have sizes of 5.0 ± 0.6 µm. The material without preheating (Figure 2c,d) shows defects and distinct boundaries between grains (similar to that in dried starch slurry).[38] These flaws in the material with no preheating correlate with lower stiffness (286 ± 71 MPa) and strength (1.07 ± 0.04 MPa). This is explained by the fact that amylopectin does not gelatinize at temperatures below ≈80 °C.[4] Preheating allows the grains to merge and produces stronger interactions between the matrix and fibers. The material preheated at T_{Pre} = 80 °C shows merged boundaries between granules, but still with defects (Figure 2e,f). The material preheated at 120 °C has minimal defects (Figure 2g,h). These observations correlate with the trends in mechanical properties at the different preheating levels.

Using the optimized preheating temperature from DOE (T_{Pre} = 120 °C), we then printed tensile specimens from

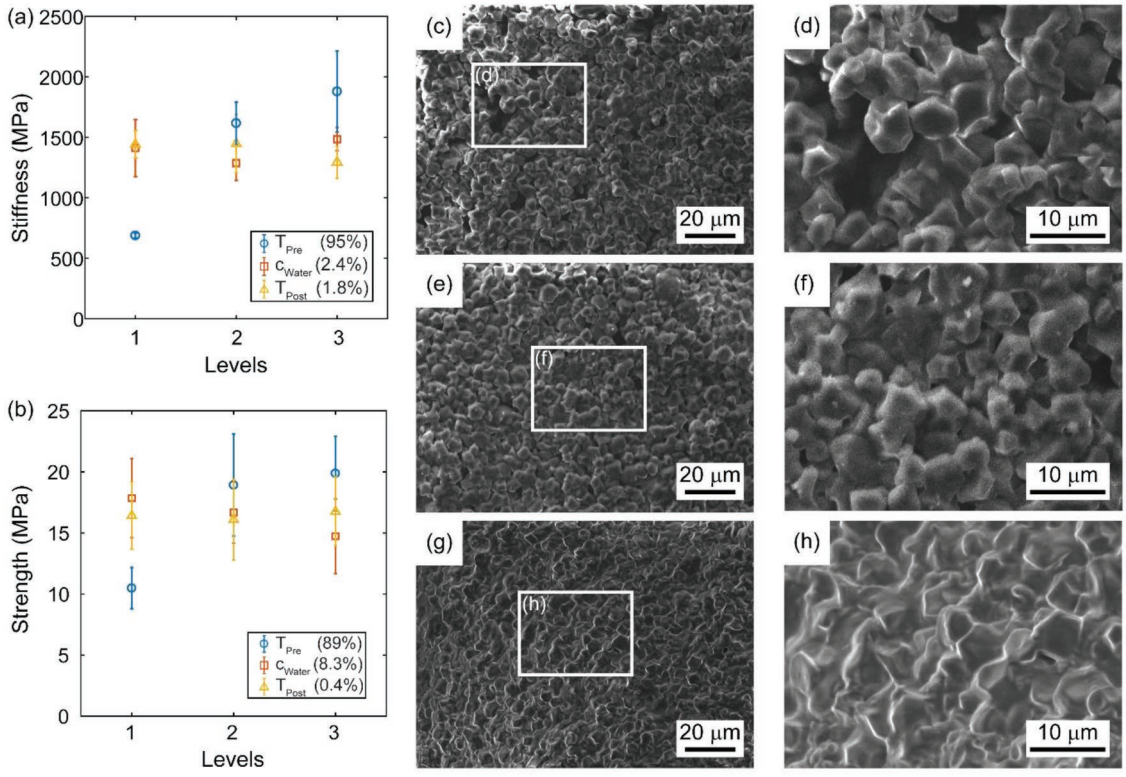

Figure 2. Effect of processing parameters on (a) stiffness and (b) strength. The values in parentheses are the percentage contribution for each parameter. SEM observations of printed samples (c,d) without preheating (micron size defects and clear boundaries between granules), (e,f) preheated at 80 °C (merged boundaries between granules, but defects are still observed), and (g,h) preheated at 120 °C (merged boundaries and minimal defects).

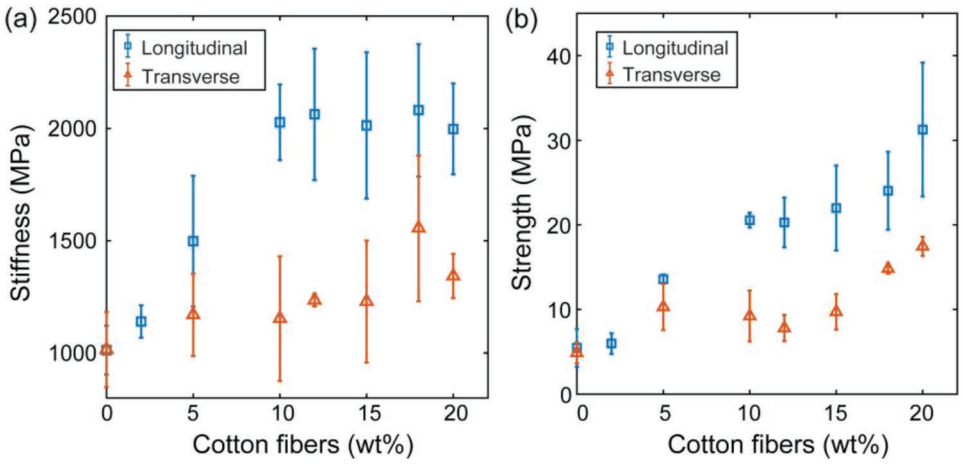

Figure 3. a) Stiffness and (b) strength of SR-based materials as a function of cotton fiber weight fraction, based on quasistatic tests performed on tensile specimens.

SR-based composites with different fiber fractions. In addition to printing samples using longitudinal print paths as above, we also printed samples with transverse print paths (i.e., to orient the primary cotton fibers perpendicular to the loading direction). The results of these tensile tests are shown in **Figure 3**. As expected for short fiber composites, samples with fibers oriented perpendicular to the loading direction have a lower overall stiffness, and only a small increase in stiffness with increasing fiber fraction. In contrast, the stiffness of samples with fibers oriented parallel with the loading direction increases significantly with increasing fiber fraction. This classic trend is observed for fiber concentrations of 0–10 wt%. Above this, the stiffness appears to reach a plateau as a function of fiber fraction. This may be related to increasing nonuniformity of mixing as the fiber fraction increases. The strength increases nominally monotonically with increasing fiber fractions (Figure 3b). For example, the strength at 20 wt% fibers is 63% larger than that at 10 wt%. The retrogradation of amylopectin ensures stability in the ambient environment for reasonable lengths of time. For example, there was no statistically significant change in mechanical properties over the maximum length period studied (one week).

Figure 4 shows SEM observations of printed SR-CL composites. A near-surface fiber is shown in Figure 4b, which is nominally aligned with the print path due to the shearing of the material as it passes through the nozzle.[31] Figure 4c shows a fracture surface (perpendicular to the printing direction), with primary cotton fibers (measured diameters of 10.9 ± 1.89 μm) emerging from the surface. Figure 4d shows both primary and the secondary fibers that emerge from them, in this case for a SR-CL20 sample. Two primary fibers can be seen aligned along the printing direction, which is horizontal in this panel (Figure 4d), with secondary fibers emerging from each primary fiber (dashed area). Interestingly, though the large primary fibers are always observed (Figure S3, Supporting Information), the secondary fiber network only forms if gelatinization and retrogradation of the amylopectin molecules occurs (which, from above, requires preheating at or above 80 °C). Without gelatinization, the secondary fibers remain part of the primary bundles (see the surface of the fiber bundles in Figure S3a, Supporting Information). During heat treatment and gelatinization, the gel balls expand and subsequently recrystallize back to a helical structure. This reorganization of the matrix could play a key role in reordering the secondary fibers. Figure S3b (Supporting Information) shows the fracture surface of a printed SR-CL10 composite, for which no thermal treatment was applied during material preparation (and hence for which no gelatinization of the amylopectin occurred). In contrast, Figure S3c (Supporting Information) shows the fracture surface of a SR-CL10 composite, which has been gelatinized via heat treatment, resulting in a large amount of secondary fibers emerging from the primary fibers. This increases the fiber–matrix surface area, which is associated with enhancement of both stiffness and strength.

To demonstrate scalability of the materials processing and possible applications, we printed standard hexagonal and triangular cellular structures (**Figure 5**a), as commonly used in traditional lightweighting[39] and as validation for new 3D printable materials.[31,40–42] Samples with varying relative densities were printed by systematically changing unit cell size and beam width. Compressive, in-plane stress–strain curves are shown in Figure S4a (Supporting Information) for SR-CL20 cellular materials with various relative densities. As expected, these experiments indicate that the toughness, stiffness, and strength all increase with increasing relative density for all composite materials (SR-CL20 in Figure 5b–d and SR-CL10 in Figure S5, Supporting Information). We also observe that at large relative densities, the failure transitions from brittle-like failure (at lower densities) to ductile-like failure (at higher densities), requiring much larger strain before catastrophic failure occurs (Figure S4a, Supporting Information). Rather than cracks propagating through the entire sample once initiated, the cellular materials with high relative density experience a layer-by-layer densification process (Figure S4b, Supporting Information). The samples with larger relative density may be less sensitive to surface flaws due to the proportionally larger cross-section of composite material.

The stiffness, E, and strength, σ, of the cellular structures can be compared to the classical cellular mechanics scaling

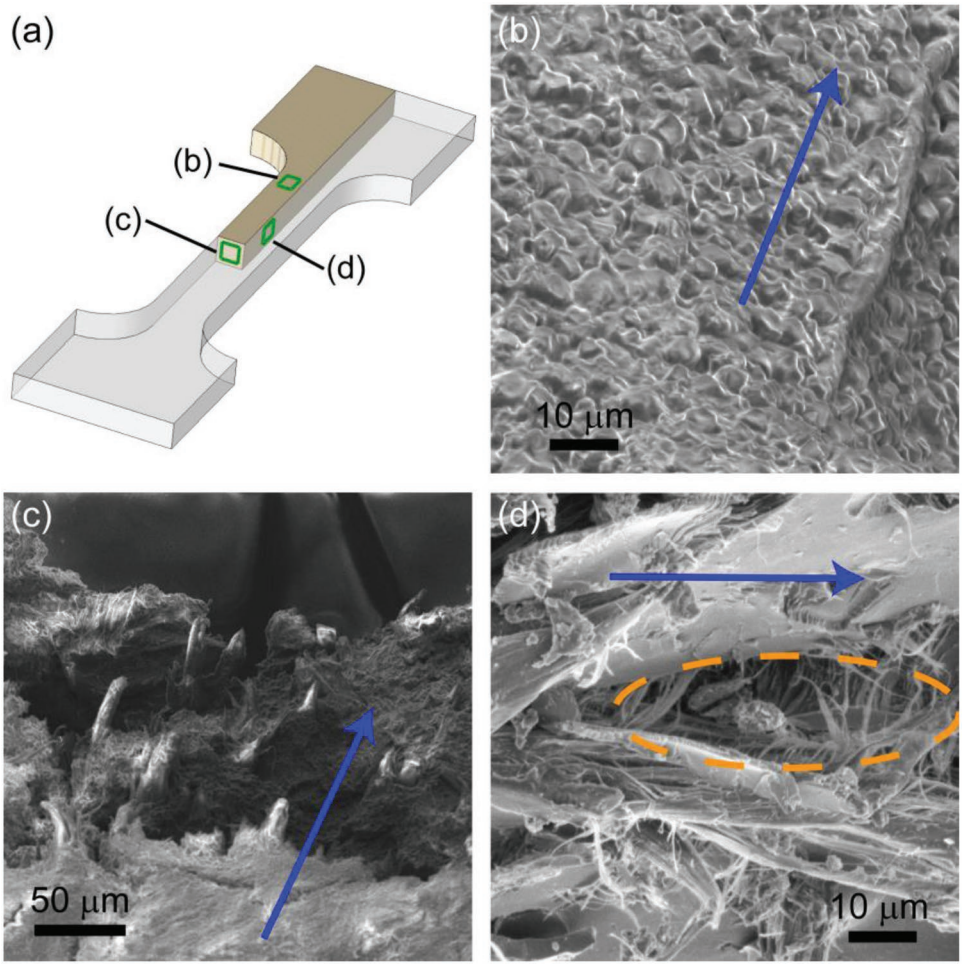

Figure 4. a) A schematic of locations of SEM observations. b) There is a notable granular appearance to the surface of the SR-CL10 composite. c) Fracture surfaces of a SR-CL10 sample show alignment of primary cotton fibers along printed direction. d) Secondary fibers emerge from the primary fibers, becoming distributed between the primary fibers as seen in the SR-CL20 samples (circled region). The blue arrows indicate the printing direction.

laws (Figure 5c,d and Figure S5a,b, Supporting Information), i.e.,

$$E = B\left(\rho / \rho_s\right)^b E_s \tag{1}$$

$$\sigma = C\left(\rho / \rho_s\right)^c \sigma_s \tag{2}$$

where $B = 1/3$, $b = 1$, $C = 1/3$, and $c = 1$ for triangular, and $B = 3/2$, $b = 3$, $C = 1/3$, and $c = 2$ for hexagonal unit cells.[39] E_S, σ_S, and ρ_S are the stiffness, strength, and density of the solid material, respectively (as measured earlier via tensile specimens). The stiffness follows the scaling law well for both SR-CL20 and SR-CL10 materials (Figure 5c and Figure S5a, Supporting Information). The measured strength, however, is generally higher than that predicted by the scaling law (Figure 5d and Figure S5b, Supporting Information), especially for hexagonal samples. Note that the classic scaling laws are derived based on the assumption that materials are isotropic. However, we used the experimentally determined orthotropic materials properties (Figure 3) in finite element analysis (FEA) and found minimal deviation from the scaling laws (Figure S6a,b, Supporting Information). The better than anticipated strength is attributed to the rounded nodes (Figure 5a), which inevitably result during extrusion due to the limited resolution of the printing method and the finite acceleration of the nozzle as it changes directions. The rounded nodes enhance strength without significantly influencing the stiffness. We confirmed the effect of nodal rounding using FEA (Figure S6a,b, Supporting Information). The simulations show that without rounded nodes the samples match the scaling law. With increasing radius of curvature ($r^* = r/w$, geometric parameters defined in Figure S6a, Supporting Information) at the nodes, both stiffness and strength increase, though stiffness increases much less than strength. At higher densities, this effect is more pronounced (Figure S6b, Supporting Information), similar to the experiments (Figure 5d). The contours in Figure S6c,d (Supporting Information) show the stress distribution in the cellular structure at 1% compressive strain for samples with $w = 8$ mm, and $r^* = 0$ and 1, respectively. Without rounded nodes (Figure S6c, Supporting Information), the stress concentrations are large at the nodes leading to premature failure of the sample (e.g., the sample in Figure S6c (Supporting Information) fails at 1.1% compression). Rounded nodes reduce these stress concentrations and distribute the

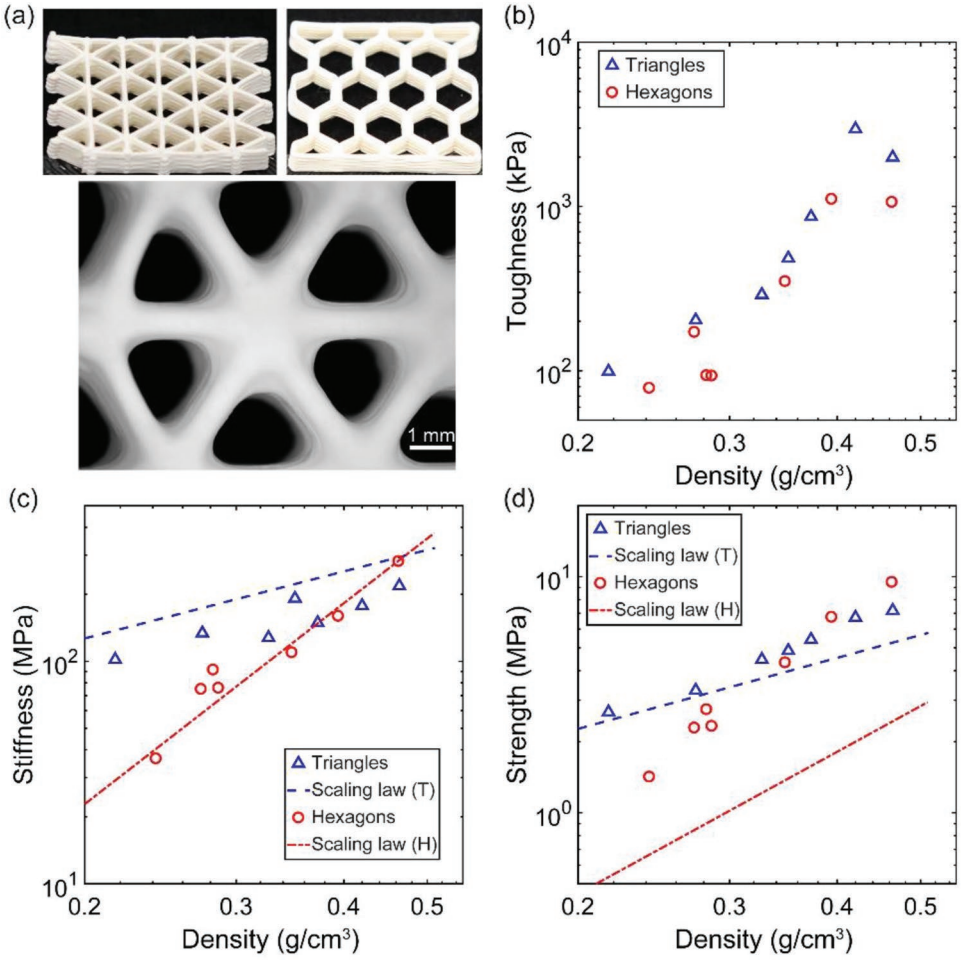

Figure 5. a) Triangular- and hexagonal cellular structures and measurements of their (b) toughness, (c) stiffness, and (d) strength as a function of density (using SR-CL20). The classical scaling laws (based on assumptions that the material is isotropic and the nodes have no rotational rigidity) are indicated by the dashed lines in (c,d) (Equations (1) and (2)).

strain more uniformly (e.g., Figure S6d (Supporting Information) shows a sample with rounded nodes that fails at 1.55% compressive strain, with a ≈92% improvement in strength).

We also compared our SR-based materials with commercial polylactic acid (PLA)-wood fiber composites. PLA is a biodegradable thermoplastic and one of the most commonly printed materials used in fused deposition modeling (FDM). However, it has known vulnerabilities to flame,[43,44] heat, and UV. We ignited the samples by holding a flame directly underneath them for 8 s. After removal of the flame, the PLA-wood fiber composites continued to burn, consuming most of the material (Figure S7a,b and Movie S1, Supporting Information). We subjected the SR-based materials to the same ignition conditions (Figure S7c,d and Movie S2, Supporting Information) and found that the fire died quickly after removal of the flame, leaving behind only surface damage. The SR-based sample remained intact and was still able to support a mechanical load. Similarly, we exposed both materials to elevated temperatures (100 and 150 °C for 30 min). Upon cooling, we performed tensile tests on these samples, which revealed that the PLA-wood composites had mechanical properties that were permanently degraded, including a 31.4% decline in stiffness and a 22.2% decline in strength (Figure S8a, Supporting Information). In contrast, the SR-based composites showed less decline in mechanical properties as a result of the elevated temperature. Stiffness and strength decreased by 12.5% and 16.9%, respectively, after thermal treatment. Finally, we measured the degradation of the materials from exposure to UV (Figure S8b, Supporting Information). After four cycles of UV exposure (300 s at 0.28 W cm^{-2} per cycle), the stiffness and strength decreased by 40% and 28.7%, respectively, for the PLA-wood composites; the stiffness and strength decreased by 16.4% and 19.3%, respectively, for the SR-based composites. The normalization was based on the values before thermal or UV treatments for PLA-based and SR-based materials, respectively (stiffness is 1815 ± 9 and 2027 ± 168 MPa, and the strength is 46 ± 7.5 and 20.6 ± 0.88 MPa, for PLA-based and SR-based materials, respectively).

Previous work indicates that starch-based materials should biodegrade faster than PLA-based materials in a controlled aerobic environment.[45] This work indicated that 50% degradation of starch-based materials should take place after 10 days and 87% degradation after 90 days. Due to the similarity between starch (both amylose and amylopectin) and SR materials

(amylopectin) similar trends are expected, though further investigation is required.

The use of natural materials in additive manufacturing has the benefit of promoting sustainability and reusability. As a final step, we demonstrated that the SR-based composites are recyclable and reusable. Through several steps of mixing, heating, and hydration (Table 1), previously printed SR materials could be recycled and re-gelatinized. This procedure is almost identical to the initial preparation steps for producing new SR materials for printing, as described in the Experimental Section. Following this procedure, we printed tensile bars from the recycled SR-based materials as a proof of concept and these exhibited comparable mechanical properties (within the margin of experimental uncertainty). In contrast, in order to reuse thermoplastics for FDM printing, such as the PLA-composites discussed above, the materials need to be melted and reformed into a coil of filament.

3. Conclusion

In summary, we have developed sticky rice (amylopectin)-based natural fiber composites and devised the materials processing steps that allow these materials to be 3D printed using conventional direct ink writing processes in ambient conditions. We have conducted a formal design of experiments to characterize how the processing parameters affect the mechanical properties of the printed materials, revealing that the preprocessing temperature T_{pre} is most important. We observe via SEM that the change in the mechanical properties resulting from the different preheating temperatures is associated with distinct microstructures (i.e., the degree of gelatinization of the SR granules). The natural fibers produce two distinct length scales of fibrous reinforcement, with thicker primary fibers aligning due to shear during printing, and secondary finer fibers that emerge from the primary fibers (but only when a sufficient T_{pre} is used, which also allows gelatinization of the amylopectin matrix to occur). The additional secondary fiber network increases the surface area between the fibers and the matrix and may thereby contribute to the strength of the composite. We have fabricated cellular materials with varying densities. The in-plane stiffness of the cellular structures follows the classical scaling law; however the strength is higher than expected (which is partly explained by the nodal rounding of the cellular structures, which reduce geometric stress concentration). Finally, we have compared the ability of the SR-based composites to withstand flame, high temperatures, and UV exposure to that of PLA-based composites, and found superior resistance to degradation in all cases.

4. Experimental Section

Materials and Preparation: The composites consist of sticky rice and cotton fibers. Amylopectin, the primary component of SR, is a highly branched polymer with a high molecular weight.[3] The branched chains are helical structures that are crystalline (at room temperature) due to a high degree of hydrogen bonding. To prepare printable inks, SR powder (Erawan Co., LTD), cotton linter (Arnold Grummer's), and water were added in the ratios shown in Table 1. The particular ratios were chosen to achieve the rheological needs for smooth printing. Then they were first mixed in vacuum at 1000 rpm for 1 min and 2000 rpm for 2 min using a FlackTek SpeedMixer. Water was added to compensate for the portion that evaporated during vacuum mixing and then mixed again using a capped bottle. Finally, the ink was heated at either 80, 100, or 120 °C for 6.5 min to allow gelatinization[4] of the amylopectin.

Fabrication: Direct ink writing was used to 3D print the cellular materials and tensile specimens. After the material was prepared as described above, it was loaded into a syringe and centrifuged at 3400 rpm for 3 min. Extrusion of the material was controlled volumetrically using a Nordson Ultra 2800. A 3D translation stage (ShopBot) was used to control the print path. Nozzles of diameter 400 and 610 µm were used.

After printing, a solidification process was used to dry the materials and allow branch chain retrogradation (recrystallization to helical structures).[3] The samples were first frozen, detached from the substrate, and then dried in a vacuum chamber for 10 min at room temperature, followed by a heat treatment at 120 °C for 45–70 min, depending on sample size and geometry. Samples were then placed in vacuum twice for 10 min. The water loss during the drying process is shown in Table S2 (Supporting Information). The multistep solidification process is critical for avoiding dimensional changes that lead to cracking during the (nonuniform) evaporation of water. The described freezing and vacuum procedures are the key to this.

μCT confirms that there is porosity in the samples after post-processing, and that the surface-to-volume ratio has a large effect on the degree of porosity (Figure S9, Supporting Information).

Rheological Characterization: The rheology of the printing materials was measured using a conventional rheometer (TA Instruments AR2000). Continuous shear rate ramp and stress sweep tests were performed at ambient temperature using a 20 mm parallel plate with a 500 µm gap size.

Mechanical Characterization: Tensile/compression tests were performed using an Instron 5564 system in displacement control at a nominal strain rate of 0.2% s^{-1}. The machine compliance was calibrated by digital image correlation (DIC) and negligible differences in strain were found between the cross head displacement and the material displacement as measured by DIC (Figure S10, Supporting Information). DIC data was processed by GOM Correlate 2017 v2.0.1 and Matlab code ncorr.m v1.2.2.

Characterization of Microstructure: SEM (JEOL-7500) was applied to observe the microstructure of the composites. X-ray computed microtomography (μCT, Scanco μCT 35) was used for characterization of porosity. The scans of cross sections across 160 µm in height were performed at a resolution of 4 µm for each sample. The porosities were calculated by integrating through the cross-section images using the built-in software.

Supporting Information

Supporting Information is available from the Wiley Online Library or from the author.

Acknowledgements

This research was partially supported by NSF through the University of Pennsylvania Materials Research Science and Engineering Center (MRSEC) (DMR-1720530) and by a 3M non-tenured faculty award. The authors thank Lu Yan and Prof. Karen I. Winey for use of the tensile testing machine, Jonathan H. Galarraga and Prof. Jason A. Burdick for use of and assistance with the rheometer, Wei-Ju Tseng and Prof. Xiaowei S. Liu for use of and assistance with μCT, and Chengyang Mo for assistance with DIC.

Conflict of Interest

The authors declare no conflict of interest.

Keywords

direct ink writing, hierarchical microstructure, natural composites, sustainable manufacturing

Received: June 22, 2019
Revised: August 22, 2019
Published online: September 23, 2019

[1] F. Yang, B. Zhang, Q. Ma, *Acc. Chem. Res.* **2010**, *43*, 936.
[2] Y.-B. Luo, Y.-J. Zhang, *Heritage Sci.* **2013**, *1*, 26.
[3] L. Yu, G. Christie, *J. Mater. Sci.* **2005**, *40*, 111.
[4] H. Liu, L. Yu, F. Xie, L. Chen, *Carbohydr. Polym.* **2006**, *65*, 357.
[5] F. Xie, L. Yu, B. Su, P. Liu, J. Wang, H. Liu, L. Chen, *J. Cereal Sci.* **2009**, *49*, 371.
[6] P. Zhao, M. D. Jackson, Y. Zhang, G. Li, P. J. M. Monteiro, L. Yang, *Constr. Build. Mater.* **2015**, *84*, 477.
[7] C. R. Rambo, N. Travitzky, K. Zimmermann, P. Greil, *Mater. Lett.* **2005**, *59*, 1028.
[8] C. X. F. Lam, X. M. Mo, S. H. Teoh, D. W. Hutmacher, *Mater. Sci. Eng., C* **2002**, *20*, 49.
[9] S. A. Khaled, J. C. Burley, M. R. Alexander, C. J. Roberts, *Int. J. Pharm.* **2014**, *461*, 105.
[10] A. S. Gladman, E. A. Matsumoto, R. G. Nuzzo, L. Mahadevan, J. A. Lewis, *Nat. Mater.* **2016**, *15*, 413.
[11] S. Chandrasekaran, E. B. Duoss, M. A. Worsley, J. P. Lewicki, *J. Mater. Chem. A* **2018**, *6*, 853.
[12] S. Sultan, A. Mathew, *Nanoscale* **2018**, *10*, 4421.
[13] A. Le Duigou, M. Castro, R. Bevan, N. Martin, *Mater. Des.* **2016**, *96*, 106.
[14] N. A. Nguyen, S. H. Barnes, C. C. Bowland, K. M. Meek, K. C. Littrell, J. K. Keum, A. K. Naskar, *Sci. Adv.* **2018**, *4*, eaat4967.
[15] Z. N. Azwa, B. F. Yousif, A. C. Manalo, W. Karunasena, *Mater. Des.* **2013**, *47*, 424.
[16] L. J. Gibson, *J. R. Soc., Interface* **2012**, *9*, 2749.
[17] V. A. Alvarez, A. Vázquez, *Polym. Degrad. Stab.* **2004**, *84*, 13.
[18] L. M. Matuana, S. Jin, N. M. Stark, *Polym. Degrad. Stab.* **2011**, *96*, 97.
[19] A. Athijayamani, M. Thiruchitrambalam, U. Natarajan, B. Pazhanivel, *Mater. Sci. Eng., A* **2009**, *517*, 344.
[20] M. F. Rosa, B. sen Chiou, E. S. Medeiros, D. F. Wood, T. G. Williams, L. H. C. Mattoso, W. J. Orts, S. H. Imam, *Bioresour. Technol.* **2009**, *100*, 5196.
[21] A. Walther, J. V. I. Timonen, I. Díez, A. Laukkanen, O. Ikkala, *Adv. Mater.* **2011**, *23*, 2924.
[22] O. Faruk, A. K. Bledzki, H. P. Fink, M. Sain, *Prog. Polym. Sci.* **2012**, *37*, 1552.
[23] A. Le Duigou, A. Kervoelen, A. Le Grand, M. Nardin, C. Baley, *Compos. Sci. Technol.* **2014**, *100*, 152.
[24] A. Iwatake, M. Nogi, H. Yano, *Compos. Sci. Technol.* **2008**, *68*, 2103.
[25] D. Regina, H. J. C. Voorwald, M. Odila, H. Cioffi, M. Lúcia, C. P. Silva, T. Gouvêa, C. Saron, *Compos. Sci. Technol.* **2009**, *69*, 214.
[26] A. Awal, M. Rana, M. Sain, *Mech. Mater.* **2015**, *80*, 87.
[27] S. Panthapulakkal, A. Zereshkian, M. Sain, *Bioresour. Technol.* **2006**, *97*, 265.
[28] D. Rouison, M. Sain, M. Couturier, *Compos. Sci. Technol.* **2004**, *64*, 629.
[29] M. Ibrahim, N. S. Badrishah, N. Sa'ude, M. H. I. Ibrahim, *App. Mech. Mater.* **2014**, *607*, 65.
[30] M. M. Kabir, H. Wang, K. T. Lau, F. Cardona, *Composites, Part B* **2012**, *43*, 2883.
[31] B. G. Compton, J. A. Lewis, *Adv. Mater.* **2014**, *26*, 5930.
[32] Y. Jiang, L. M. Korpas, J. R. Raney, *Nat. Commun.* **2019**, *10*, 128.
[33] J. A. Lewis, *Adv. Funct. Mater.* **2006**, *16*, 2193.
[34] J. R. Raney, J. A. Lewis, *MRS Bull.* **2015**, *40*, 943.
[35] R. L. Truby, J. A. Lewis, *Nature* **2016**, *540*, 371.
[36] J. R. Raney, B. G. Compton, J. Mueller, T. J. Ober, K. Shea, J. A. Lewis, *Proc. Natl. Acad. Sci.* **2018**, *115*, 1198.
[37] G. Taguchi, S. Chowdhury, Y. Wu, *Taguchi's Quality Engineering Handbook*, Wiley-Interscience, Hoboken, New Jersey **2004**.
[38] L. Goehring, *Phys. Rev. E* **2009**, *80*, 36116.
[39] N. A. Fleck, V. S. Deshpande, M. F. Ashby, *Proc. R. Soc. A* **2010**, *466*, 2495.
[40] S. Malek, J. R. Raney, J. A. Lewis, L. J. Gibson, *Bioinspiration Biomimetics* **2017**, *12*, 026014.
[41] J. T. Muth, P. G. Dixon, L. Woish, L. J. Gibson, J. A. Lewis, *Proc. Natl. Acad. Sci. USA* **2017**, *114*, 1832.
[42] J. Maurath, N. Willenbacher, *J. Eur. Ceram. Soc.* **2017**, *37*, 4833.
[43] M. García, J. Hidalgo, I. Garmendia, J. García-Jaca, *Composites, Part A* **2009**, *40*, 1772.
[44] A. B. Morgan, C. A. Wilkie, *Flame Retardant Polymer Nanocomposite*, John Wiley & Sons, Hoboken, New Jersey **2007**.
[45] R. Iovino, R. Zullo, M. A. Rao, L. Cassar, L. Gianfreda, *Polym. Degrad. Stab.* **2008**, *93*, 147.

ADVANCED MATERIALS TECHNOLOGIES

Supporting Information

for *Adv. Mater. Technol.*, DOI: 10.1002/admt.201900521

3D Printing of Amylopectin-Based Natural Fiber Composites

*Yijie Jiang and Jordan R. Raney**

Supporting Information

3D printing of amylopectin-based natural fiber composites

*Yijie Jiang and Jordan R. Raney**

Dr. Yijie Jiang, Prof. Jordan R. Raney
Department of Mechanical Engineering and Applied Mechanics, University of Pennsylvania, Philadelphia, PA 19104, USA
E-mail: raney@seas.upenn.edu

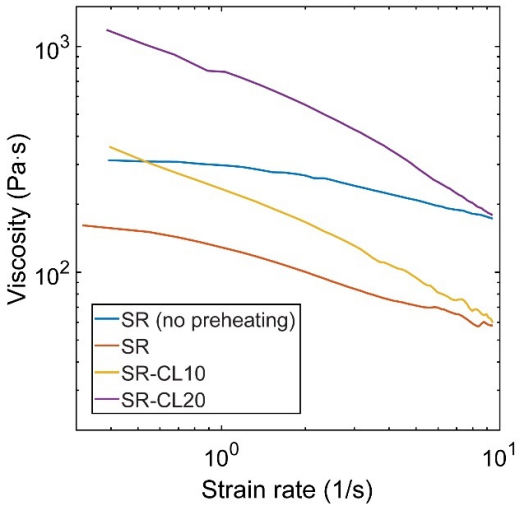

Figure S1. Pure SR (with and without preheating), SR-CL10, and SR-CL20 inks are all shear-thinning.

Printability map and Taguchi DOE

SR-CL10 inks were prepared with varying water content (C_{Water}) and preheating temperatures (T_{Pre}) shown in Figure S2, and then loaded into 10 cc syringes with 610 μm nozzles. The printable inks (green region in Figure S2) were able to be printed at 20 mm/s and to be stacked to multiple layers (usually 4-6 layers for a tensile bar). As C_{Water} decreased, the inks were printable only at low speeds (<5 mm/s) and would often clog the nozzle (orange), and eventually could not extrude (red). With more water (blue), the inks do not maintain their shape after extrusion. The pure SR ink (without fibers) can be printed by 250 μm nozzles. However, the addition of fibers causes significant clogging, and requires nozzles with diameter of at least 400 μm for reliable printing.

Taguchi DOE were performed with three parameters (T_{Pre}, C_{Water}, and T_{Post}) and three levels for each parameter as listed in Table 2. Nine sets of specimens were manufactured and experiments were carried out according to Table S1. An analysis of variables (ANOVA) process was used for evaluation of the results. Of these parameters, T_{Pre} is the most important

contributor to both stiffness (95%) and strength (89%). F-test with α=0.05 confirms the significance of T_{Pre}.

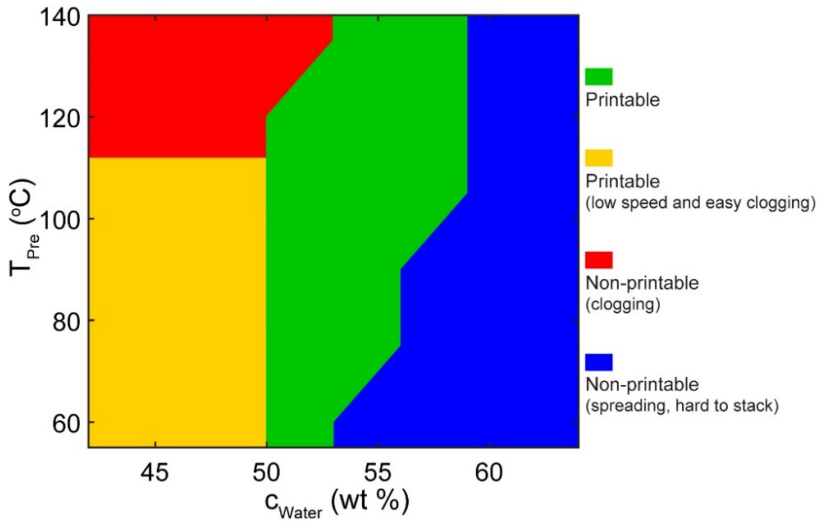

Figure S2. Printability map of SR-CL10 ink for varying preheating temperature and initial water content.

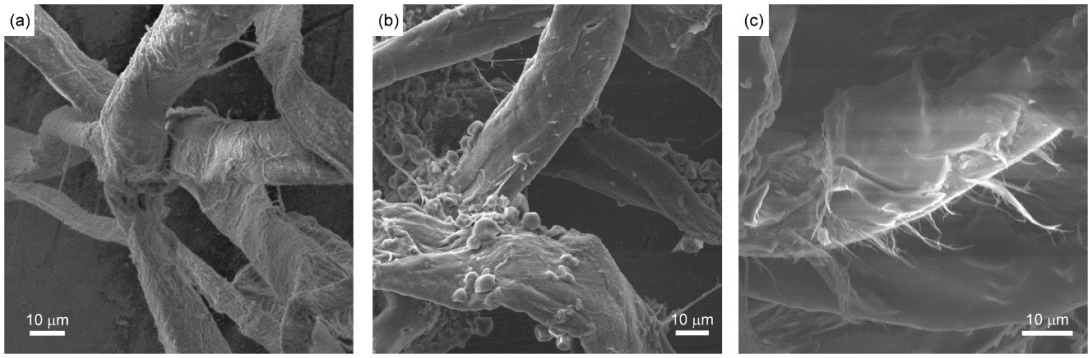

Figure S3. (a) SEM image of cotton fibers without SR. The thin secondary fibers remain tangled along the surfaces of the thick primary fibers. (b) Mix of cotton fibers and SR without heating. There is still almost no emergence of secondary fibers from the primary fibers. (c) With sufficient T_{pre}, the secondary fibers clearly emerge from the primary fibers in SR-CL composites, greatly increasing the surface area between fiber and matrix.

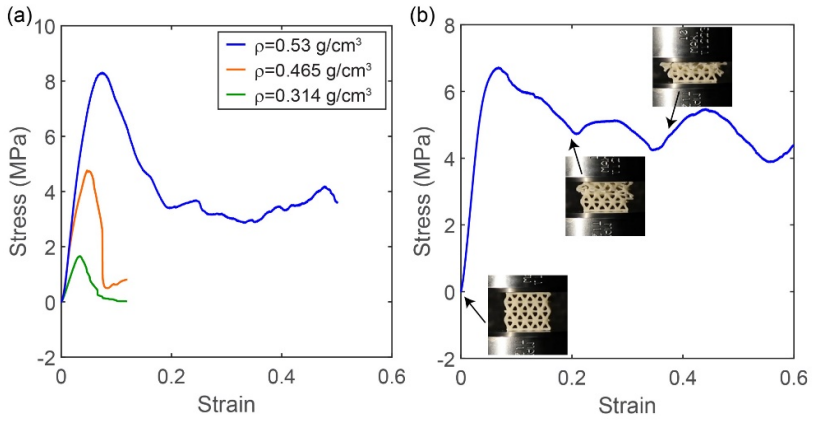

Figure S4. (a) Example stress-strain curves for in-plane compression of SR-CL20 cellular structures of varying density, (b) in-plane compression of a specimen with high toughness, together with screenshots of the sample collapsing, indicating a layer-by-layer densification process.

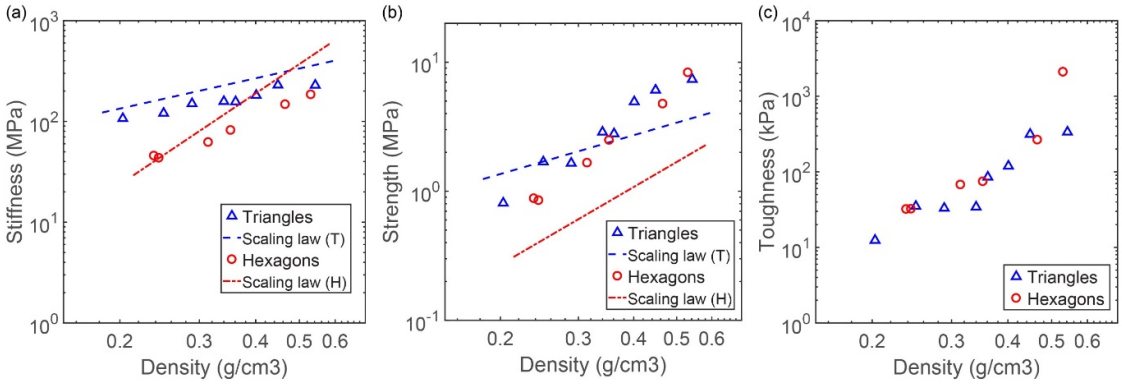

Figure S5. (a) Stiffness, (b) strength, and (c) toughness of SR-CL10 cellular samples as a function of density.

Finite element analysis (FEA)

FEA was performed to understand the stiffness and strength of cellular materials. A quarter of a unit cell of hexagonal cellular materials with edge length l=25 mm and varying width w=4-15 mm was used in Abaqus® v6.9. Symmetric boundary conditions were used to ensure the models represent whole cells properly. The relative density ρ/ρ_s varied from 0.18 to 0.57,

which was similar to that in experiments. Experimental specimens do not show the sharp features at a strut-node junction that would be expected in the idealized geometry. Rather, the nodes are rounded. We used FEA to examine the effect of this rounding on stiffness and strength. The dimensions used were $r^*=0$ (i.e., the idealized cellular geometry with no nodal rounding), 0.5, and 1, where $r^*=r/w$. Orthotropic material properties were applied (i.e., elastic modulus and failure stress were defined differently along longitudinal and transverse directions using experimentally-measured tensile data from the SR-CL20 composites). A displacement boundary condition was applied to compress the models until any element reached the failure stress, at which point the simulation would stop. Force-displacement curves were then output, and stiffness and strength of the models were calculated to compare with scaling laws.

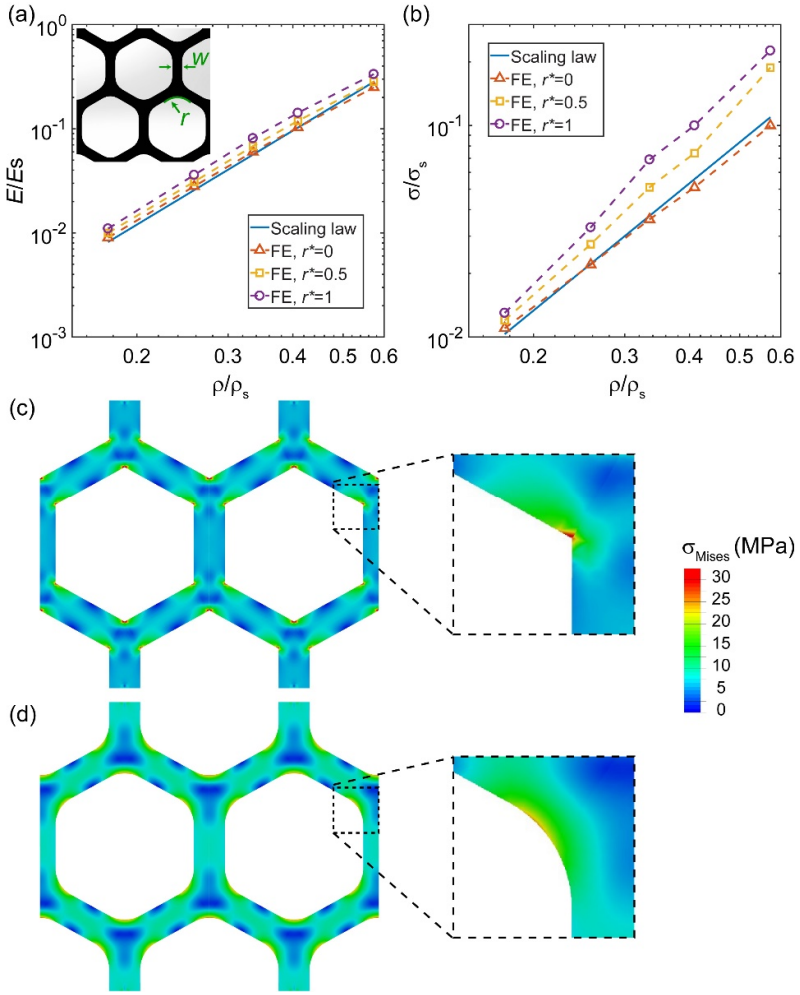

Figure S6. FE simulations of cellular samples with varying density and different degrees of rounding at the nodes. (a-b) Comparison of the classic scaling law and the FEA results of stiffness and strength as a function of relative density for hexagonal samples with and without rounded corners. Stress contour on cellular structures (c) without rounded corner and (d) with rounded corner (r*=1) at 1% nominal strain in vertical direction.

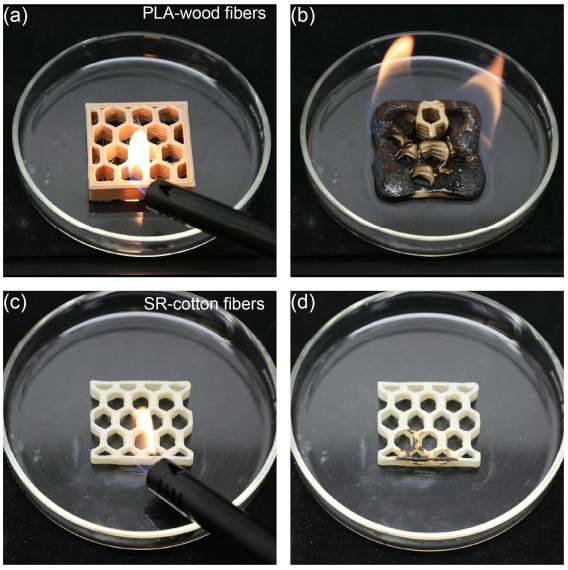

Figure S7. (a) A PLA-wood fiber sample is ignited at its edge for ~8 s and (b) the fire continues to burn and damage the whole PLA-wood fiber sample, while (c) a SR-CL sample under the same conditions (ignition for ~8 s) is sufficiently fire retardant that (d) the flame dies quickly and only causes surface damage.

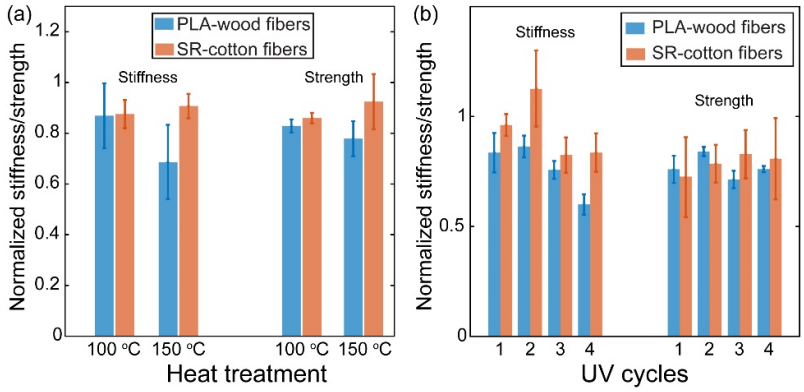

Figure S8. Effect of (a) thermal treatment and (b) UV treatment on mechanical properties of SR-CL and PLA-wood fibers composites. (a) Each thermal treatment (either 100 or 150 ^{o}C as indicated) lasted 30 min, with the mechanical testing occurring after the samples returned to room temperature. Stiffness and strength were reduced by 31.4% and 22.2%, respectively for the PLA-wood fiber composite; the stiffness and strength was reduced by 12.5% and 16.9%, respectively for the SR-CL composite. (b) Each UV cycle is 300 s under 0.28 W/cm^2 UV

exposure. After four cycles, the stiffness and strength was reduced by 40% and 28.7%, respectively, for the PLA-wood fiber composite; stiffness and strength was only reduced by 16.4% and 19.3%, respectively, in SR-CL composites.

Porosities of samples with different surface to volume ratios

The surface to volume ratio has a significant effect on the microstructure as a result of its effects on the drying kinetics. Correspondingly, the porosities of the samples increase from 4.73% to 31.2% (based on X-ray computed micro-tomography, μCT, presented in Figure S9a-b) as the surface to volume ratio is increased from 0.88 to 2.31 mm^{-1}. Figure S9a-b show stiffness and strength of samples with different surface to volume ratios. With increasing surface to volume ratio, both properties decrease significantly. The degree of these effects could be mitigated via additives to alter the surface tension of the water; however, we did not investigate this further in this study.

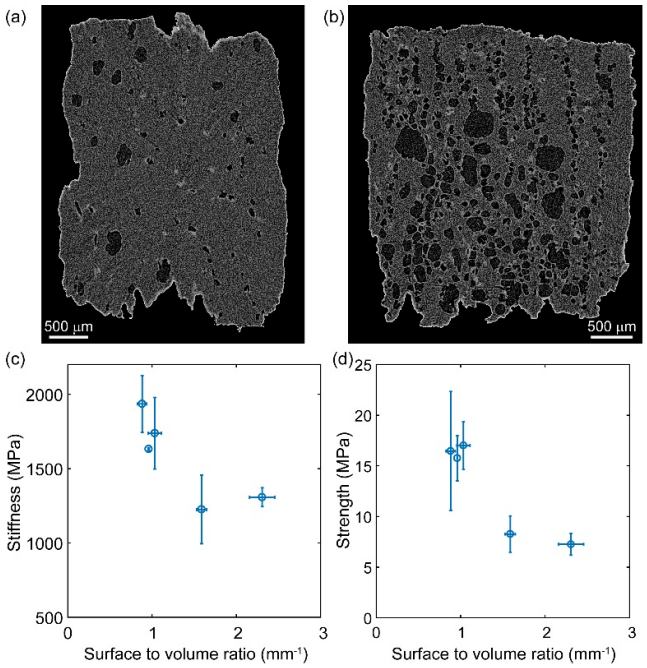

Figure S9. (a-b) μCT observation of pores in samples with different surface to volume ratios. The porosity and surface to volume ratio are (a) 4.73% and 0.88 mm^{-1} and (b) 31.2% and 2.31 mm^{-1}. Effect of surface to volume ratio on (c) stiffness and (d) strength of SR-CL10 materials.

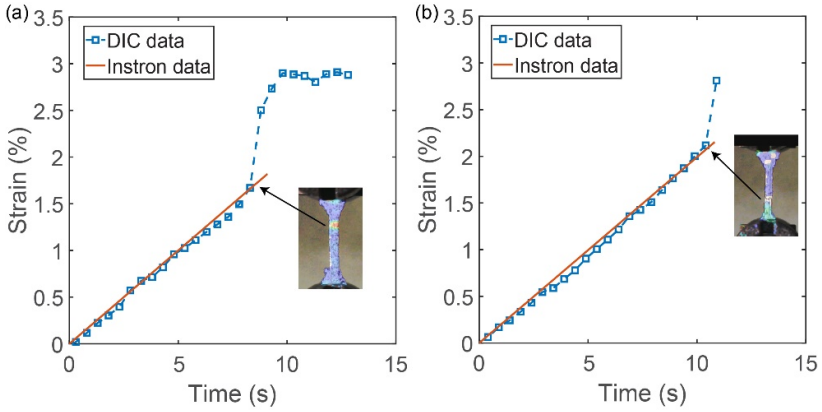

Figure S10. (a-b) Strain calculated from crosshead displacement in a commercial quasistatic test system (Instron) and from DIC for two SR-CL10 samples. The observed discrepancy occurs only after the samples fracture.

Table S1. The L9 orthogonal array for Taguchi DOE.

Case #	T_{Pre} (^{o}C)	C_{Water} (wt%)	T_{Post} (^{o}C)
1	80	50	90
2	80	53	120
3	80	56	150
4	100	50	150
5	100	53	90
6	100	56	120
7	120	50	120
8	120	53	150
9	120	56	90

Table S2. Weight variation of SR-CL10 samples during the solidification process. The reduction of the weight is 48.9±0.51 wt%.

Sample #	Initial mass (g)	Vacuum	Heat	Vacuum	Vacuum	Mass reduced (%)
1	2.02	1.88	1.06	1.03	1.02	49.5
2	1.98	1.83	1.05	1.01	1	49.49
3	2.01	1.87	1.07	1.03	1.03	48.76
4	2.2	2.03	1.17	1.14	1.13	48.64
5	1.95	1.84	1.06	1.01	1.01	48.21